

# All-optical reconfiguration of far-field singularities in a photonic-crystal laser

Abhishek Padhy,<sup>1,2</sup> Zhiyi Yuan,<sup>3,4</sup> Mohammed Hamdad,<sup>1</sup> Panagiotis Nianios,<sup>1</sup> Romane Houvenaghel,<sup>1</sup> Aziz Benamrouche,<sup>1</sup> Nicolas Roy,<sup>2</sup> Thanh Phong Vo,<sup>1</sup> Christian Seassal,<sup>1</sup> Xavier Letartre,<sup>1</sup> Lotfi Berguiga,<sup>1</sup> Michaël Lobet,<sup>2</sup> Ségolène Callard,<sup>1</sup> and Hai Son Nguyen<sup>1,4,5,\*</sup>

<sup>1</sup>*Ecole Centrale de Lyon, CNRS, INSA Lyon, Université Claude Bernard Lyon 1, CPE Lyon, Institut des Nanotechnologies de Lyon (INL), UMR 5270, 69130 Écully, France*

<sup>2</sup>*Department of Physics, University of Namur, Rue de Bruxelles 61, 5000 Namur, Belgium*

<sup>3</sup>*Centre for OptoElectronics and Biophotonics (COEB),*

*School of Electrical and Electronic Engineering, Nanyang Technological University, Singapore 639798*

<sup>4</sup>*CNRS-International-NTU-Thales Research Alliance (CINTRA), IRL 3288, Singapore*

<sup>5</sup>*Institut Universitaire de France (IUF), France*

(Dated: February 20, 2026)

Singular optics has emerged as an important research area with diverse applications, yet controlling optical singularities in nanophotonic emitters is typically limited by fixed subwavelength geometries and diffraction-limited control. Here, we circumvent this limitation and demonstrate an all-optical mechanism for reconfiguring far-field singularities in a photonic crystal laser. The underlying principle involves optical pumping, which creates a mesoscopic potential landscape whose spatial variations are slow compared to the lattice period. Such a potential localizes a Bloch band into trapped states whose envelope functions, and thus far-field singularity textures, are defined by the pump geometry. Using a honeycomb PhC that supports a symmetry-protected bound state in the continuum, we achieve room-temperature telecom-band lasing with real-space polarisation singularities that are reconfigurable in both number and position, while the intrinsic momentum-space singularity at the  $\Gamma$ -point is preserved. The experimental observations align quantitatively with an analytical framework that combines the Bloch mode of the structure and envelope function theory, establishing envelope engineering as a versatile route to programmable singular-light emission in active photonic lattices.

## INTRODUCTION

Optical singularities, points where the phase or polarization of light is undefined, play a central role in structured-light physics and carry quantized topological charges [1, 2]. Their control underpins applications in robust communication [3, 4], precision metrology [5], and vortex lasing [6–9]. In nanophotonics, such singularities may be imposed externally through phase engineering or arise intrinsically from the eigenmodes of resonant metasurfaces and photonic crystals (PhCs). Bound states in the continuum (BICs), whose radiation vanishes by symmetry or interference, provide a powerful route to generating singular beams directly from photonic resonances [7, 10–12].

Achieving dynamic control of these singularities remains challenging because the far-field texture of a Bloch mode is fixed by the unit-cell geometry, and conventional structures offer little reconfigurability. Thermal tuning in phase-change PhCs allows switching between BIC lasing modes with different topological charges [13], and photoisomerization in organic PhCs provides a similar mode-switching mechanism [14], but neither approach can reshape the singularity texture of a given Bloch resonance. Recent optical-control schemes modulate refractive in-

dex at the unit-cell scale: ultrafast pumping can destroy BIC singularities by breaking in-plane symmetries [8], and gain-loss perturbations suppress vortex emission [9, 15]. Sub-unit-cell pumping can even alter the response of individual elements [16], but remains limited to passive linewidth tuning and does not enable continuous control of far-field singularities. Fundamentally, all these schemes attempt to reconfigure the unit cell, an operation constrained by the diffraction limit. In this work, we introduce an alternative approach, instead of modifying the subwavelength Bloch function, we reconfigure the mesoscopic envelope of a PhC resonance using optical pumping (see Fig. 1). Carrier injection creates a smooth in-plane potential that localizes a Bloch band into trapped states whose envelope functions obey a two-dimensional Schrödinger equation, which can be shaped arbitrarily by the pump profile. Because the radiated field is the product of the Bloch-mode far field and its envelope, this mechanism enables reconfigurable far-field singularities without altering the photonic crystal itself.

As a proof of concept, we use a honeycomb PhC supporting the lowest-energy band with isotropic negative-mass dispersion and a monopolar BIC at the  $\Gamma$ -point ( $\mathbf{k}_{\parallel} = \mathbf{0}$ ). Optical pumping forms tunable potentials that trap this band and yield lasing trapped states whose real-space far-field polarization singularities can be programmed by the pump geometry, whereas the momentum-space singularity remains fixed. Lasing occurs at room temperature and telecom wavelengths, and

\* [hai-son.nguyen@ec-lyon.fr](mailto:hai-son.nguyen@ec-lyon.fr)

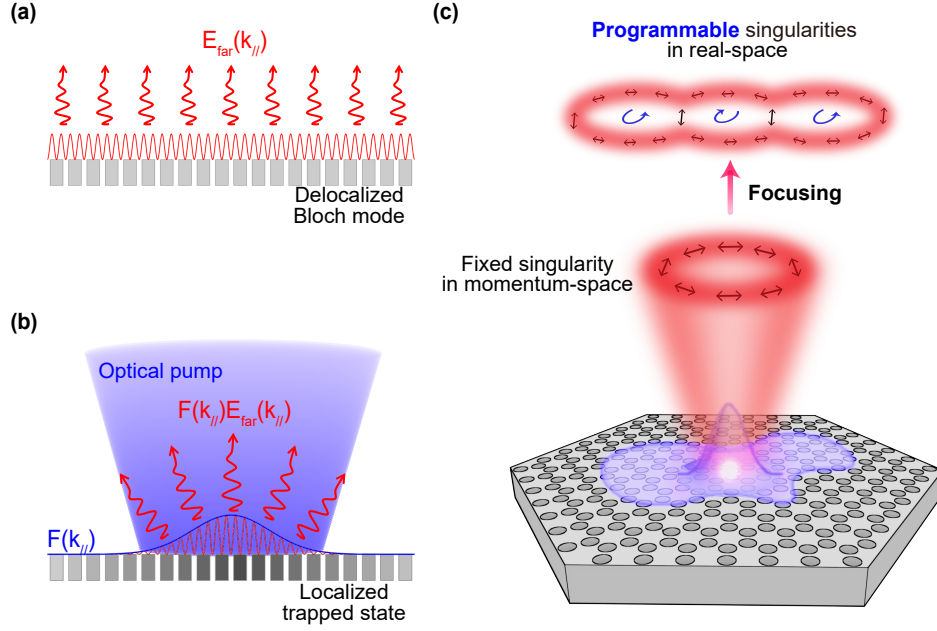


Figure 1. **Concept:** (a) In the absence of pumping, a Bloch resonance of a PhC slab is delocalized over the lattice and radiates into the continuum with a fixed momentum-space far-field pattern  $\mathbf{E}_{\text{far}}(\mathbf{k}_{\parallel})$ . (b) A shaped optical pump injects carriers and creates a smooth in-plane potential that localizes the Bloch band into a trapped state with envelope  $F(\mathbf{r}_{\parallel})$ . In momentum space, the trapped-state emission inherits the Bloch-mode topology but is modulated by the envelope spectrum,  $\mathbf{E}_{\text{far}}^{\text{trap}}(\mathbf{k}_{\parallel}) \propto F(\mathbf{k}_{\parallel})\mathbf{E}_{\text{far}}(\mathbf{k}_{\parallel})$ . (c) Schematic of the all-optical control of the photonic crystal laser with singularities. The far-field singularities in the real-space can be controlled by the optical pump.

the measurements agree quantitatively with envelope-function theory, establishing a general route to reconfigure singular beams in active photonic lattices.

## RESULTS

### Theoretical framework

We first consider the generic guided resonances of a PhC slab in the absence of optical pumping. For a fixed in-plane wave vector  $\mathbf{k}_{\parallel} = (k_x, k_y)$ , the corresponding Bloch mode inside the slab can be expanded over a finite set of basis consisting of guided modes of an effective homogeneous slab, each carrying a reciprocal lattice vector  $\mathbf{G}_n$ . The guided modes in the basis share the same out-of-plane profile  $u(z)$  and differ only in their in-plane Bloch harmonics. Factoring out the global Bloch phase  $e^{i\mathbf{k}_{\parallel} \cdot \mathbf{r}_{\parallel}}$  for compactness, the near field can be written as  $\mathbf{E}_{\text{near}, \mathbf{k}_{\parallel}}(\mathbf{r}_{\parallel}, z) = u(z) \sum_n A_n(\mathbf{k}_{\parallel}) e^{i\mathbf{G}_n \cdot \mathbf{r}_{\parallel}} \mathbf{p}_n$ , where  $\mathbf{r}_{\parallel} = (x, y)$  denotes the in-plane coordinate,  $\{\mathbf{p}_n\}$  are the polarization of the guided-mode basis. Here,  $A_n(\mathbf{k}_{\parallel})$  are the expansion coefficients obtained by diagonalizing the effective non-Hermitian Hamiltonian of the PhC slab [17]. Radiation into the continuum is obtained by projecting this Bloch mode onto the outgoing Fabry-Pérot channel of the unpatterned slab (Fig. 1(a)). In the single-channel regime relevant here (subwavelength

lattice, thus the zeroth diffraction order inside the light cone is the only leaky channel), the radiated field in direction  $\mathbf{k}_{\parallel}$  is proportional to the same guided-mode coefficients, but without the fast lattice harmonics  $e^{i\mathbf{G}_n \cdot \mathbf{r}_{\parallel}}$  [17]:  $\mathbf{E}_{\text{far}}(\mathbf{k}_{\parallel}) \propto \left[ \sum_n A_n(\mathbf{k}_{\parallel}) \mathbf{p}_n \right] \sqrt{\gamma(\mathbf{k}_{\parallel})}$ , where  $\gamma(\mathbf{k}_{\parallel})$  is the radiative loss rate of the Bloch resonance. The polarization texture and the existence of BICs are encoded in the vector  $\sum_n A_n(\mathbf{k}_{\parallel}) \mathbf{p}_n$ , whereas  $\gamma(\mathbf{k}_{\parallel})$  sets the emitted intensity. The complex eigenfrequency of the guided resonance can be described as  $\omega(\mathbf{k}_{\parallel}) \simeq \omega_0 + \frac{\hbar^2 |\mathbf{k}_{\parallel}|^2}{2m} - i\gamma(\mathbf{k}_{\parallel})$ , where  $m$  is the effective mass of the Bloch resonance. In general, the photonic band can exhibit anisotropy, but here, the guided resonances have been chosen such that the effective mass  $m$  is negative and isotropic. Under optical pumping, photogenerated carriers produce a carrier-induced optical nonlinearity that leads to a spatially varying refractive-index change  $\Delta n(\mathbf{r}_{\parallel}) < 0$  [18]. This smooth index decrease maps onto an effective in-plane blueshift potential  $V(\mathbf{r}_{\parallel})$  for the Bloch band [19, 20], thereby trapping the lowest-energy states in a pump-defined landscape. Within the effective-mass approximation, and neglecting losses in the in-plane eigenproblem for small  $\gamma(\mathbf{k}_{\parallel})$ , the in-plane dynamics are governed by a standard Hermitian Schrödinger equation for the envelope function  $F(\mathbf{r}_{\parallel})$ :  $-\frac{\hbar^2}{2m} \nabla_{\mathbf{r}_{\parallel}}^2 F(\mathbf{r}_{\parallel}) + V(\mathbf{r}_{\parallel}) F(\mathbf{r}_{\parallel}) = E F(\mathbf{r}_{\parallel})$ . Because  $m < 0$ , a positive potential  $V(\mathbf{r}_{\parallel})$  has a

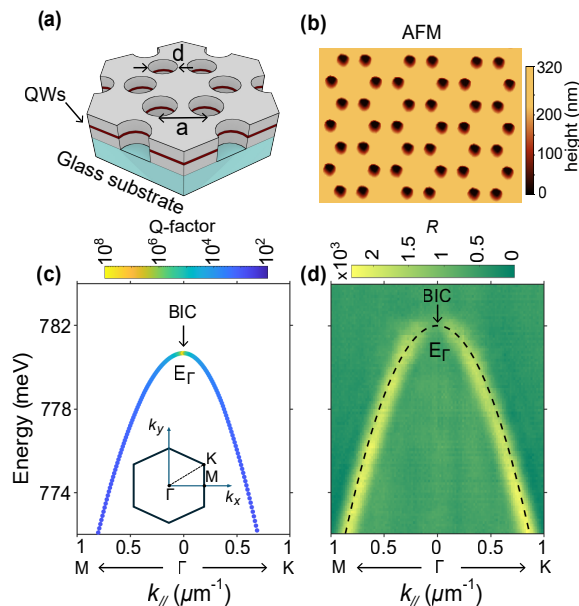


Figure 2. **The fabricated photonic crystal device and its dispersion:** (a) Schematic of the fabricated honeycomb PhC slab. The lattice has a period  $\Lambda = a\sqrt{3}$  with lattice constant  $a = 445$  nm, hole diameter  $d = 335$  nm, and total membrane thickness  $t = 240$  nm. (b) Atomic-force-microscopy (AFM) image of the fabricated surface. (c) Numerically computed band structure using Legume, showing the lowest-energy band that hosts a monopolar symmetry-protected BIC at the  $\Gamma$ -point. The band is nearly isotropic and displays a negative effective mass. (d) Experimental angle-resolved photoluminescence along the  $\Gamma$ -K and  $\Gamma$ -M directions, exhibiting the vanishing radiative loss at  $\Gamma$  which is characteristic of the BIC. The dashed line represents a parabolic fit to the measured dispersion.

confining effect and localizes light under the pump spot, forming trapped states. Each trapped state corresponds to a solution  $F(\mathbf{r}_{\parallel})$  of the Schrödinger equation given above; its Fourier transform  $F(\mathbf{k}_{\parallel}) = \text{FT}[F(\mathbf{r}_{\parallel})]$  specifies how the Bloch resonances are superposed in momentum space. The near field of a trapped state can thus be written as a superposition of Bloch modes weighted by  $F(\mathbf{k}_{\parallel})$ :

$$\mathbf{E}_{\text{near}}^{\text{trap}}(\mathbf{r}_{\parallel}) = \sum_{\mathbf{k}_{\parallel}} F(\mathbf{k}_{\parallel}) \mathbf{E}_{\text{near},\mathbf{k}_{\parallel}}(\mathbf{r}_{\parallel}, z), \quad (1)$$

or, in the continuum limit, as an integral over  $\mathbf{k}_{\parallel}$ . The corresponding far field of the trapped state in momentum space is

$$\mathbf{E}_{\text{far}}^{\text{trap}}(\mathbf{k}_{\parallel}) = F(\mathbf{k}_{\parallel}) \mathbf{E}_{\text{far}}(\mathbf{k}_{\parallel}), \quad (2)$$

that is, the original Bloch far-field pattern is modulated by the envelope spectrum  $F(\mathbf{k}_{\parallel})$  [see Fig. 1(b)]. Finally, the far field of the trapped state in real space is obtained by the inverse Fourier transform of Eq. (2) as follows:

$$\mathbf{E}_{\text{far}}^{\text{trap}}(\mathbf{r}_{\parallel}) = \text{FT}^{-1}[F(\mathbf{k}_{\parallel}) \mathbf{E}_{\text{far}}(\mathbf{k}_{\parallel})]. \quad (3)$$

Equations (1)–(3) make the central mechanism explicit: the singularities of the radiated field are dictated jointly by the Bloch resonance, through  $\mathbf{E}_{\text{far}}(\mathbf{k}_{\parallel})$ , and by the pump-induced envelope, through  $F(\mathbf{k}_{\parallel})$ . The Bloch contribution determines the intrinsic momentum-space topology carried by the underlying band, whereas the envelope reshapes the distribution of momenta and thereby controls the number, position, and structure of the singularities in the real space.

A special case arises when the underlying Bloch resonance is a symmetry-protected BIC. Since such modes satisfy  $\mathbf{E}_{\text{far}}(\mathbf{k}_{\parallel} = \mathbf{0}) = \mathbf{0}$ , Eq. (2) ensures that any trapped state constructed from them also obeys  $\mathbf{E}_{\text{far}}^{\text{trap}}(\mathbf{k}_{\parallel} = \mathbf{0}) = \mathbf{0}$ , regardless of the envelope function. The momentum-space singularity at  $\Gamma$ -point is therefore preserved under arbitrary optical pumping. In contrast, the real-space far field of the trapped state is given by Eq. (3), can exhibit a wide variety of polarization patterns and singularity textures, set by the geometry of the pump-induced potential and the resulting envelope function  $F(\mathbf{r}_{\parallel})$ .

### Proof of Concept

To demonstrate envelope-function control experimentally, we use a two-dimensional honeycomb photonic crystal slab patterned into an InP/InAsP/InP multiple-quantum-well membrane [Fig. 2(a–b)]. The heterostructure is grown by molecular beam epitaxy, the active InP-based membrane is molecularly bonded onto a glass substrate, and the PhC is defined by electron-beam lithography followed by reactive-ion etching.

Numerical band-structure calculations were performed using the guided-mode-expansion solver Legume [21], together with angle-resolved photoluminescence measurements [Fig. 2(c–d)](see Methods for setup details), show that the lowest-energy band of the fabricated honeycomb PhC is perfectly isotropic and follows a parabolic dispersion with negative effective mass. At the  $\Gamma$ -point, this band hosts a symmetry-protected monopolar BIC, evidenced by the vanishing radiative loss  $\gamma(\mathbf{k}_{\parallel}) \propto |\mathbf{k}_{\parallel}|^2$  [Fig. 2(c–d)]. A full analytical description of this Bloch resonance, including the effective non-Hermitian Hamiltonian and its eigenmodes, is provided in Methods. In the following, we use this band to engineer the trapped states, whose envelope function is entirely shaped by the optical pump.

The sample was excited using a femtosecond laser at 800 nm, shaped by a spatial light modulator (SLM). The pump was focused on a single Gaussian spot on the PhC slab [Fig. 3(a)], injecting carriers into the InP/InAsP/InP multiple-quantum-well membrane and creating a smooth refractive-index blue-shift that acts as a confining potential for the lowest-energy Bloch band. This potential can be modeled as  $V(\mathbf{r}_{\parallel}) = V_0 e^{-|\mathbf{r}_{\parallel}|^2/\sigma^2}$ ,

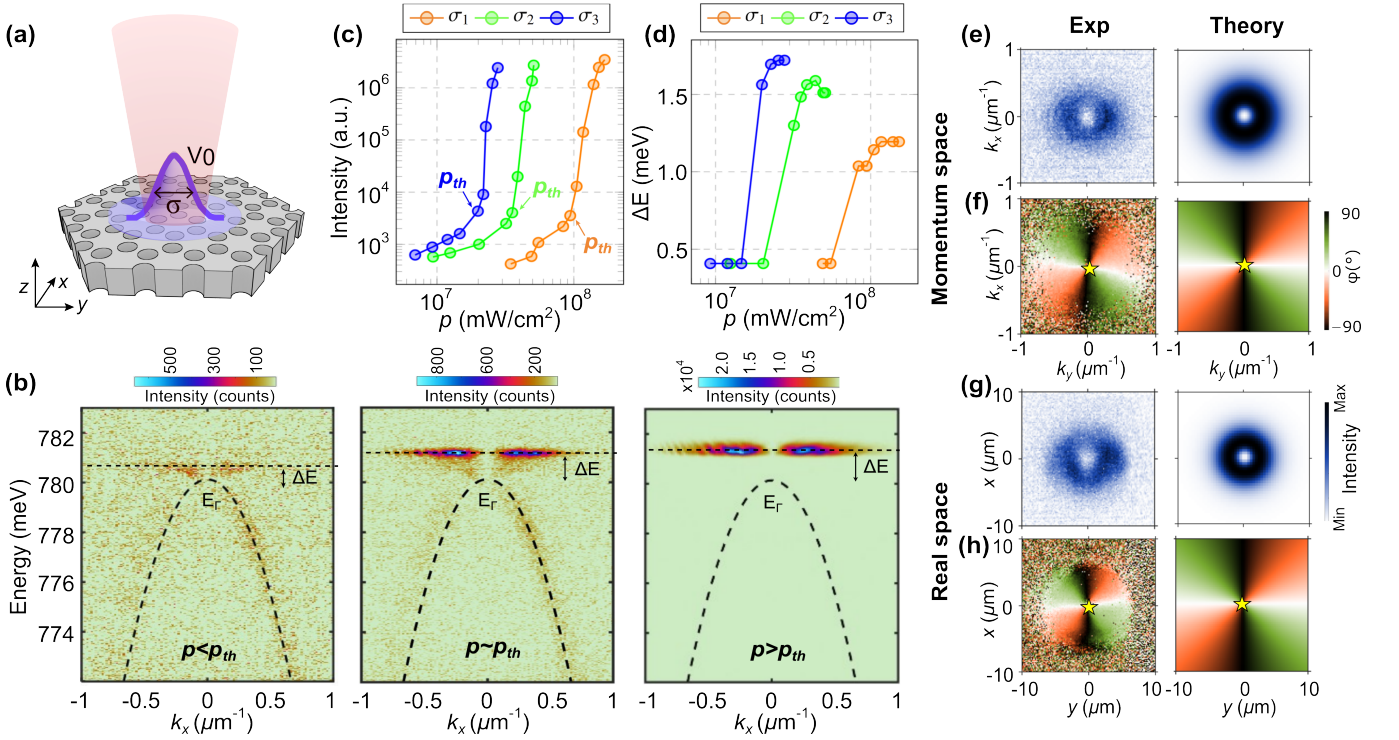


Figure 3. **Lasing characterization and farfield measurements for single pump spot:** (a) Schematic of single spot pumping on the PhC with spot size  $\sigma$ . The pump creates a potential  $V(\mathbf{r}_{\parallel})$ , which induces a trapped-state envelope function  $F(\mathbf{r}_{\parallel})$ . (b) Experimental energy-momentum dispersion along  $k_x$  below ( $p < p_{th}$ ), around ( $p \sim p_{th}$ ) and above threshold ( $p > p_{th}$ ) pump power density ( $p$ ) for spot waist  $\sigma_1 = 3.2\mu\text{m}$ . The fundamental mode is fitted with a parabola with  $\alpha = -13.4\text{ meV}\cdot\mu\text{m}^2$ , and the confinement energy ( $\Delta E$ ) is the difference between the trapped mode energy and energy at  $\Gamma$ -point ( $E_{\Gamma}$ ). (c) Total integrated trapped-state intensity vs pump power density  $p$  for three pump waists  $\sigma_1 = 3.2\mu\text{m}$ ,  $\sigma_2 = 7.1\mu\text{m}$ ,  $\sigma_3 = 11.1\mu\text{m}$ . (d) Confinement energy  $\Delta E$  vs pump power for the three spot waists. (e–h) Far-field characterization of the trapped state above threshold for  $\sigma = 3.2\mu\text{m}$ . Panels show (left) experimental momentum-space and real-space intensity and polarization textures and (right) corresponding analytical predictions from the envelope-function model. The yellow stars mark the polarization singularities. The theoretical results were calculated with the parameter  $V_0 = 4.8\text{ meV}$ . [Refer Extended Fig.A1 for the polarization resolved farfield lasing images.]

where the depth  $V_0$  is set by the injected carrier density, and the trap size  $\sigma$  is controlled precisely by the SLM.

Figure 3(b) shows the measured dispersion with increasing pump power density. At low pump power density, the emission follows the unperturbed band with inverted parabolic dispersion  $E(k_x) = E_{\Gamma} + \alpha k_x^2$ ; a fit gives  $\alpha = -13.4\text{ meV}\cdot\mu\text{m}^2$ , confirming the negative effective mass. Upon increasing the pump power, a dispersionless line appears above  $E_{\Gamma}$ , indicating the formation of a trapped state with confinement energy  $\Delta E$ . The blueshift of the trapped mode increased with the pump power below the threshold because the additional injected carriers deepened the effective confining potential. Above the lasing threshold, however, the blueshift saturates: injected carriers become clamped by stimulated emission, so additional pump power produces photons rather than increasing the carrier reservoir, fixing the confinement depth  $V_0$ , which is estimated to be approximately 4.8 meV (see Methods for evaluation of  $V_0$ ). Figures 3(c–d) quantify these behaviors.

The total flatband intensity showed a characteristic  $S$ -shaped dependence on the pump power density, demonstrating single-mode lasing. Notably, the lasing threshold decreases when the pump-spot size increases [ $\sigma_1 < \sigma_2 < \sigma_3$  in Fig. 3(c)]. A smaller excitation spot produces a broader momentum-space envelope, which overlaps more strongly with the high- $k$  components of the Bloch mode, whose radiative losses scale as  $|\mathbf{k}_{\parallel}|^2$ . As a result, the radiative loss of the trapped state scales approximately as  $1/\sigma^2$ . Therefore, small traps require a larger carrier density at the threshold to compensate for their greater radiative leakage, whereas larger traps experience weaker loss and lasing at a lower gain. The saturated confinement energy  $\Delta E$  above the threshold also increases with the pump-spot diameter [Fig. 3(d)]. Indeed, a larger  $\sigma$  creates a broader and shallower potential, and in the negative-mass Schrödinger model, the trapped-state energy shifts upward.

To investigate the far-field radiation pattern, we focus on the case  $\sigma = 3.2\mu\text{m}$  and examine the correspond-

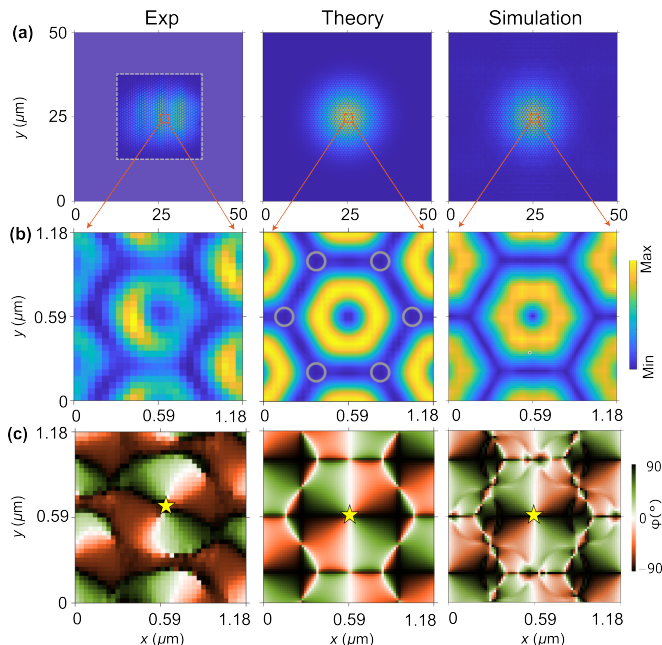


Figure 4. **Nearfield maps for single pump:** (a) Large-area SNOM (left panel), analytical model (middle), and FDTD numerical (right) of near-field map of the trapped state under a single Gaussian pump. The white dashed line box represents the measurement region. (b) Zoomed-in near-field amplitude showing the fast spatial oscillations of the Bloch resonance on the scale of the photonic crystal lattice. (c) Polarization-resolved mapping of the in-plane electric field.

ing far-field intensity and polarization textures in both momentum and real space above the threshold (the radiation patterns are the same for other spot sizes). The measurements, together with the analytical predictions of the envelope function model, are presented in Fig.3(e–h). The momentum-space lasing emission exhibits a polarization vortex centered at  $\mathbf{k}_{\parallel} = \mathbf{0}$  [Fig. 3(e–f)], characteristic of the monopolar BIC of the underlying Bloch mode [17]. As dictated by Eq. (2), the radiative amplitude vanishes at the  $\Gamma$ -point for any envelope function; therefore, the momentum-space singularity is preserved independently of the pump profile.

In contrast, the real-space far-field directly reflects the envelope of the trapped state. For the monopolar BIC, the unperturbed Bloch mode radiates as  $\mathbf{E}_{\text{far}}(\mathbf{k}_{\parallel}) \propto k_{\parallel} \mathbf{u}_{\varphi}$  [refer Eq.(A10) in Methods], so the trapped-state emission is the inverse Fourier transform of  $k_{\parallel} F(\mathbf{k}_{\parallel}) \mathbf{u}_{\varphi}$ . For a Gaussian pump spot, the envelope  $F(\mathbf{r}_{\parallel})$  is radially symmetric and peaks at the center, thus taking the form  $F(r_{\parallel})$ . Multiplication by  $k_{\parallel}$  in momentum space corresponds to taking a radial derivative in real space, yielding  $\mathbf{E}_{\text{far}}^{\text{trap}}(\mathbf{r}_{\parallel}) \propto F'(r_{\parallel}) \mathbf{u}_{\varphi}$ . Any smooth, centrally peaked envelope satisfies  $F'(0) = 0$ , producing a donut-shaped real-space intensity with a single polarization singularity, as shown in Fig. 3(g–h). These results confirm that the monopolar BIC fixes the momentum-space

topology, while the pump-defined envelope sets the real-space structure.

Near-field imaging with scanning near-field optical microscopy (SNOM) [22, 23] provides direct access to both the mesoscopic envelope and the microscopic Bloch component of the trapped state. The large-area SNOM map in Fig. 4(a) reveals a Gaussian-like intensity profile localized beneath the pump, with a maximum at the pump center and a smooth decay, in agreement with the confined state predicted by the effective-mass model. The slight elongation of the envelope is likely caused by a weak ellipticity of the excitation focus in the SNOM setup. Zoomed-in views [Figs. 4(b–c)] resolve the rapid subwavelength oscillations associated with the Bloch mode. Within each unit cell, the measured near field displays the characteristic azimuthal rotation expected for the magnetic-monopole resonance: the in-plane field winds around the hexagon center with a full  $2\pi$  phase rotation. Polarization-resolved SNOM measurements [Fig. 4(c)] further corroborate this picture, showing a clear vortex-like winding of the local electric-field vector. Together, these results demonstrate that the trapped state preserves the microscopic polarization texture of the monopolar Bloch resonance while acquiring a mesoscopic envelope dictated by the optically induced potential. The SNOM observations are in excellent agreement with both the analytical envelope-function model and full-wave finite-difference time-domain (FDTD) simulations. In the FDTD calculations, we emulate the optically induced potential by introducing a Gaussian refractive-index perturbation,  $n(\mathbf{r}_{\parallel}) = n_0 + \delta_n \exp(-|\mathbf{r}_{\parallel}|^2/\sigma^2)$ , with  $n_0 = 3.162$  and  $\delta_n = -0.022$ .

### Reconfigurable singularities

To illustrate that the far-field singularity texture can be programmed on demand, we shaped the pump into two Gaussian spots separated by a distance  $L$ , forming a diatomic photonic “molecule” [Fig. 5(a)]. Each pump spot defines an optically induced trap that plays the role of an “atom,” while their overlap enables tunnel-like coupling controlled by  $L$ . The pump waist was fixed to  $\sigma = 3.25\mu\text{m}$ , and the device was driven above the threshold into the lasing regime.

The measured energy–momentum dispersions for decreasing  $L$  are shown in Fig. 5(b). For large separations (top row), only a single trapped-state branch is visible, corresponding to two nearly independent localized states. As  $L$  decreases, coupling between the traps increases and the lasing mode splits into anti-bonding (AB) and bonding (B) branches, analogous to the molecular eigenstates of a double-well potential [24]. The dependence of their energies on  $L$  is plotted in Fig. 5(c) and agrees quantitatively with the

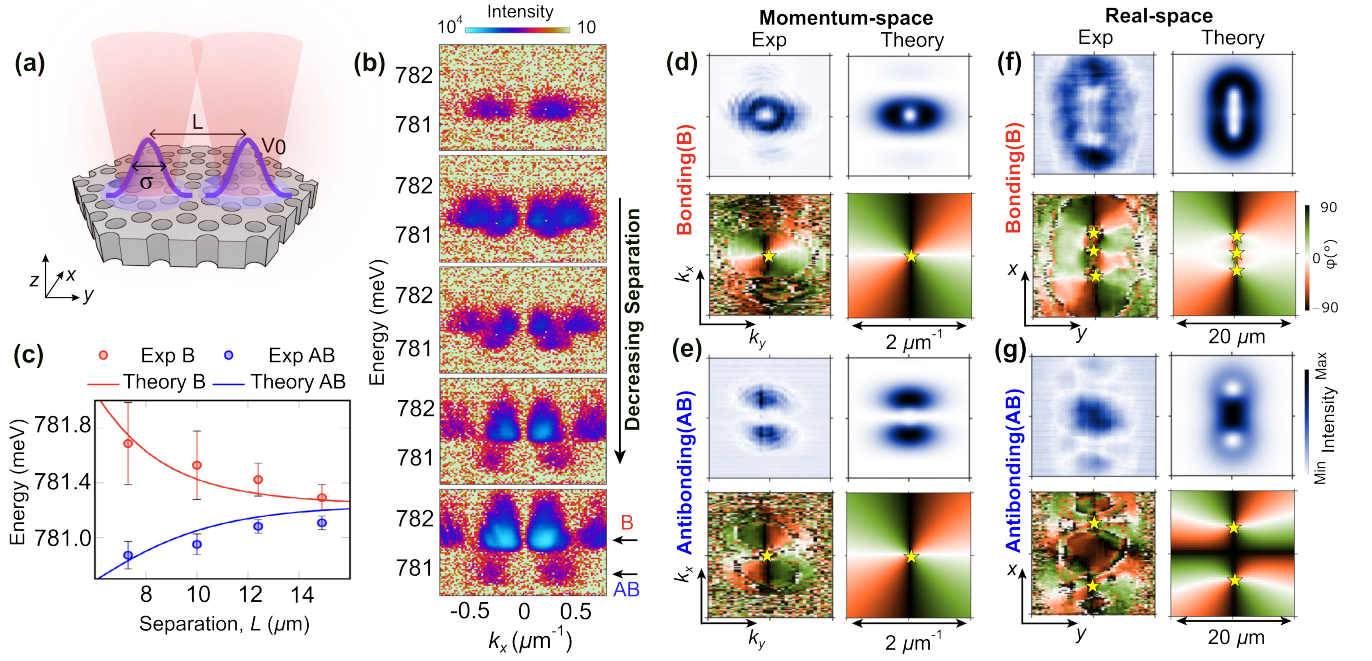


Figure 5. **Two-spot pumping and the demonstration of reconfigurable singularities in the farfield:**(a) Schematic of two trapped states induced by a double pump spot with varying separation distance  $L$  with fixed spot waist  $\sigma = 3.25\mu\text{m}$ . (b) Energy-momentum dispersion along  $k_x$  for various  $L$  (14.9, 11.9, 10.4,  $7.2\mu\text{m}$ ), decreasing from top panel ( $14.9\mu\text{m}$ ) to the bottom panel ( $7.2\mu\text{m}$ ). Far-field patterns (for  $L=7.2\mu\text{m}$ ) in momentum and real space for both Bonding (d) and Antibonding (e) modes, and the experimental results (left) are supported by the analytical/theory results (right). Singularities are denoted by yellow stars. The theoretical results are calculated with parameter  $V_0 = 4.6\text{ meV}$ . [Refer fig. A2 for the corresponding polarization resolved farfield lasing images.]

effective-mass Schrödinger model for a two-well potential  $V(x, y) = V_0 \left[ e^{-(x^2 + (y-L/2)^2)/\sigma^2} + e^{-(x^2 + (y+L/2)^2)/\sigma^2} \right]$ , using  $V_0$  obtained from the method discussed for a single spot. This establishes that the lasing branches correspond to the B and AB envelope eigenstates of pump-induced potential landscape.

Because the underlying Bloch resonance is a monopolar BIC with  $\mathbf{E}_{\text{far}}(\mathbf{0}) = \mathbf{0}$ , both B and AB modes retain a single polarization vortex pinned at  $\Gamma$ -point, as seen in the momentum-space measurements shown in Fig. 5(d–e). In real space, however, the two modes exhibit strikingly different polarization singularity structures. The AB mode shows three polarization singularities, while the B mode exhibits two [Fig. 5(f–g)]. These patterns follow directly from Eq.(3): different molecular eigenstates correspond to different envelope spectra  $F(\mathbf{k}_{\parallel})$ , which reshape the real-space radiation while leaving the  $\Gamma$ -point singularity fixed. The analytical far-field patterns evaluated from the envelope-function model [right column of Figs. 5(d–e)] match the measured vortex configurations with no adjustable parameters.

To demonstrate the scalability of envelope-function control, we also investigated a configuration using three identical pump spots arranged linearly with equal separation  $L = 13\mu\text{m}$ . The three pump spots generate a

composite potential consisting of three overlapping Gaussian wells, which supports three trapped eigenstates—the photonic analogue of the three molecular orbitals in a linear triatomic chain. These states appear as three distinct lasing modes and correspond to the three lowest solutions of the effective-mass Schrödinger equation for a triple-well potential. Extended Figure A3 compares the experimental and theoretical far-field emission patterns of the three trapped modes in both real space and momentum space, together with the associated polarization textures obtained from polarization-resolved tomography. As expected, all the three modes preserve the same momentum-space vortex at  $\Gamma$ , inherited from the monopolar BIC of the underlying Bloch resonance. In contrast, each trapped mode exhibits a distinct real-space polarization-singularity pattern determined by the nodal structure of its envelope function: the ground state (Mode 1) displays one singularity, the first excited state (Mode 2) displays two singularities, and the second excited state (Mode 3) displays three singularities. The experimental maps and analytical predictions show excellent quantitative agreement in both intensity and polarization textures, including the singularity locations indicated by the yellow stars in Extended Fig. A3.

These results demonstrate that envelope-function engineering enables reconfigurable real-space singulari-

ties—including their number, type, and position—while the momentum-space topology remains protected by the symmetry of the underlying Bloch mode. Adjusting the pump separation  $L$  continuously tunes the molecular hybridization and therefore the far-field vortex pattern. More broadly, because the effective potential is written optically, the approach naturally extends to more complex pump geometries (e.g., multi-spot arrays, asymmetric patterns, and dynamically modulated profiles), providing additional degrees of freedom to sculpt the trapped-state landscape and the resulting singularity textures on demand. This concept thus offers a scalable route to programmable singular-beam generation in active photonic crystals.

## CONCLUSION

We demonstrated an all-optical mechanism for reconfiguring far-field singularities in active photonic crystals by tailoring the mesoscopic envelope of a Bloch resonance. This approach bypasses the need to modify subwavelength unit-cell geometries and instead uses pump-induced carrier potentials to localize a Bloch band into trapped states described by a two-dimensional Schrödinger equation. In a honeycomb PhC supporting a monopolar BIC, we demonstrated that the intrinsic momentum-space singularity remains fixed, whereas the real-space polarization texture can be continuously reshaped through the envelope function. Multi-spot pumping enables trapped states hosting controllable numbers and positions of singularities, which is in quantitative agreement with the analytical theory. Because the mechanism relies solely on carrier injection, reconfiguration can, in principle, operate on picosecond timescales [19, 20, 25, 26]. Extensions toward dynamic pump modulation and programmable multi-spot pumping could enable reconfigurable tight-binding Hamiltonians for quantum simulation [27, 28] and laser-array architectures with controllable coupling for neuromorphic computing [29, 30], further expanding the possibilities of ultrafast programmable structured-light emitters.

## ACKNOWLEDGEMENTS

We thank Philippe Regreny for growing epitaxial structures. Wafer bonding technology was supplied by CEA-LETI. This work was supported by the French National Research Agency (ANR) under the projects NANOEC (ANR07-NANO-036), POLAROID (ANR-24-CE24-7616-01), and SUPER-HERO (ANR-25-CE24-4066). A. P. was supported by the LABEX iMUST of the University of Lyon through the “Stage d’Innovation 2023–24” program. A. P. dedicates this work to N. Palo and M. Palo.

## AUTHOR CONTRIBUTIONS

H.S.N. conceived the idea and developed the theoretical model. S.C., T.P.V., and C.S. fabricated the structures. A.B. and S.C. carried out the near-field (SNOM) measurements. Z.Y., X.L., and N.R. performed the FDTD simulations. L.B. contributed to the optical-bench setup and SLM characterization. A.P., H.S.N., P.N, M.H. and R.H. performed the far-field optical measurements and analyzed the experimental data in comparison with theory. H.S.N., Z.Y., S.C., M.L., and A.P. wrote the initial draft of the manuscript. All authors reviewed, edited, and approved the final version.

## COMPETING INTERESTS

The authors declare no conflicts of interest.

- 
- [1] Y. Shen, X. Wang, Z. Xie, C. Min, X. Fu, Q. Liu, M. Gong, and X. Yuan, *Light: Science & Applications* **8**, 90 (2019).
  - [2] M. S. Soskin, S. V. Boriskina, Y. Chong, M. R. Dennis, and A. Desyatnikov, *Journal of Optics* **19**, 010401 (2017).
  - [3] A. E. Willner, H. Huang, Y. Yan, Y. Ren, N. Ahmed, G. Xie, C. Bao, L. Li, Y. Cao, Z. Zhao, J. Wang, M. P. J. Lavery, M. Tur, S. Ramachandran, A. F. Molisch, N. Ashrafi, and S. Ashrafi, *Advances in Optics and Photonics* **7**, 66 (2015).
  - [4] B. Ndagano, I. Nape, M. A. Cox, C. Rosales-Guzmán, and A. Forbes, *Journal of Lightwave Technology* **36**, 292 (2018).
  - [5] M. Cheng, W. Jiang, L. Guo, J. Li, and A. Forbes, *Light: Science & Applications* **14**, 4 (2025).
  - [6] M. Hwang, H. Kim, J. Kim, B. Yang, Y. Kivshar, and H. Park, *Nature Photonics* **18**, 286 (2023).
  - [7] R. Mermet-Lyaudoz, C. Symonds, F. Berry, E. Drouard, C. Chevalier, G. Trippé-Allard, E. Deleporte, J. Bellessa, C. Seassal, and H. S. Nguyen, *Nano Letters* **23**, 4152 (2023).
  - [8] C. Huang, C. Zhang, S. Xiao, Y. Wang, Y. Fan, Y. Liu, N. Zhang, G. Qu, H. Ji, J. Han, L. Ge, Y. Kivshar, and Q. Song, *Science* **367**, 1018 (2020).
  - [9] X. Gao, G. Zhao, M. Song, and X. Ao, *Nano Letters* **24**, 10943–10948 (2024).
  - [10] B. Zhen, C. W. Hsu, L. Lu, A. D. Stone, and M. Soljačić, *Physical Review Letters* **113**, 257401 (2014).
  - [11] H. M. Doeleman, F. Monticone, W. den Hollander, A. Alù, and A. F. Koenderink, *Nature Photonics* **12**, 397 (2018).
  - [12] Y. Zhang, A. Chen, W. Liu, C. W. Hsu, B. Wang, F. Guan, X. Liu, L. Shi, L. Lu, and J. Zi, *Physical Review Letters* **120**, 186103 (2018).
  - [13] J. Tian, G. Adamo, H. Liu, M. Wu, M. Klein, J. Deng, N. S. S. Ang, R. Paniagua-Domínguez, H. Liu, A. I. Kuznetsov, and C. Soci, *Advanced Materials* **35**, 10.1002/adma.202207430 (2022).

- [14] X. Yan, M. Tang, Z. Zhou, L. Ma, Y. Vaynzof, J. Yao, H. Dong, and Y. S. Zhao, *Nature Communications* **16**, [10.1038/s41467-025-57738-1](https://doi.org/10.1038/s41467-025-57738-1) (2025).
- [15] X. Wu, S. Zhang, J. Song, X. Deng, W. Du, X. Zeng, Y. Zhang, Z. Zhang, Y. Chen, Y. Wang, C. Jiang, Y. Zhong, B. Wu, Z. Zhu, Y. Liang, Q. Zhang, Q. Xiong, and X. Liu, *Nature Communications* **15**, [10.1038/s41467-024-47669-8](https://doi.org/10.1038/s41467-024-47669-8) (2024).
- [16] A. Aigner, T. Possmayer, T. Weber, A. A. Antonov, L. de S. Menezes, S. A. Maier, and A. Tittl, *Nature* **644**, 896–902 (2025).
- [17] V. A. Nguyen, H. S. Nguyen, Z. Yuan, D. X. Nguyen, C. Dang, S. T. Ha, X. Letartre, Q. Le-Van, and H. S. Nguyen, *Nanophotonics* **14**, 5229 (2025).
- [18] B. Bennett, R. Soref, and J. Del Alamo, *IEEE Journal of Quantum Electronics* **26**, 113–122 (1990).
- [19] S. W. Leonard, H. M. van Driel, J. Schilling, and R. B. Wehrspohn, *Physical Review B* **66**, [10.1103/physrevb.66.161102](https://doi.org/10.1103/physrevb.66.161102) (2002).
- [20] I. Fushman, E. Waks, D. Englund, N. Stoltz, P. Petroff, and J. Vučković, *Applied Physics Letters* **90**, [10.1063/1.2710080](https://doi.org/10.1063/1.2710080) (2007).
- [21] S. Zanotti, M. Minkov, D. Nigro, D. Gerace, S. Fan, and L. C. Andreani, *Computer Physics Communications* **304**, 109286 (2024).
- [22] T.-P. Vo, A. Rahmani, A. Belarouci, C. Seassal, D. Nedeljkovic, and S. Callard, *Opt. Express* **18**, 26879 (2010).
- [23] T.-P. Vo, M. Mivelle, S. Callard, A. Rahmani, F. Baida, D. Charraut, A. Belarouci, D. Nedeljkovic, C. Seassal, G. Burr, and T. Grosjean, *Opt. Express* **20**, 4124 (2012).
- [24] P. W. Atkins and R. S. Friedman, *Molecular Quantum Mechanics*, 5th ed. (Oxford University Press, 2011).
- [25] Y. Yu, E. Palushani, M. Heuck, D. Vukovic, C. Peucheret, K. Yvind, and J. Mork, *Applied Physics Letters* **105**, [10.1063/1.4893984](https://doi.org/10.1063/1.4893984) (2014).
- [26] M. R. Shcherbakov, S. Liu, V. V. Zubyuk, A. Vaskin, P. P. Vabishchevich, G. Keeler, T. Pertsch, T. V. Dogva, I. Staude, I. Brener, and A. A. Fedyanin, *Nature Communications* **8**, [10.1038/s41467-017-00019-3](https://doi.org/10.1038/s41467-017-00019-3) (2017).
- [27] A. Aspuru-Guzik and P. Walther, *Nature Physics* **8**, 285–291 (2012).
- [28] T. Grass, D. Bercioux, U. Bhattacharya, M. Lewenstein, H. S. Nguyen, and C. Weitenberg, *Reviews of Modern Physics* **97**, [10.1103/revmodphys.97.011001](https://doi.org/10.1103/revmodphys.97.011001) (2025).
- [29] Z. Chen, A. Sludds, R. Davis, I. Christen, L. Bernstein, L. Ateshian, T. Heuser, N. Heermeier, J. A. Lott, S. Reitzenstein, R. Hamerly, and D. Englund, *Nature Photonics* **17**, 723–730 (2023).
- [30] K. Ji, G. Tirabassi, C. Masoller, L. Ge, and A. M. Yacomotti, *Nature Communications* **16**, [10.1038/s41467-025-64252-x](https://doi.org/10.1038/s41467-025-64252-x) (2025).
- [31] S. Cuffe, L. Berguiga, and H. S. Nguyen, *Nanophotonics* **13**, 841 (2024).

## METHODS

### Analytical model of the magnetic monopolar mode

Following the theoretical framework developed in Ref. [17], in this section we summarize the effective non-Hermitian model used to describe the magnetic monopolar mode of the honeycomb PhC slab. Near the  $\Gamma$  point, the Bloch field can be expressed as a coherent superposition of six TE-like guided harmonics associated with the first-order reciprocal-lattice vectors  $\mathbf{G}_{n=1..6}$ ,

$$\mathbf{G}_n = G, (\cos \phi_n, \sin \phi_n), \quad \phi_n = \frac{\pi}{3}(n-1), \quad (\text{A1})$$

each carrying an in-plane polarization vector  $\mathbf{p}_n = (-\sin \phi_n, \cos \phi_n)$ . All six components correspond to the same fundamental TE guided mode of the effective homogeneous slab; the lattice simply couples these harmonics through diffraction and radiations. In this basis the effective Hamiltonian reads

$$\hat{H}_\Gamma(\mathbf{k}) = \omega_\Gamma + \begin{pmatrix} v_\Gamma |\mathbf{k}_\parallel| \cos(\varphi - \frac{\pi}{3}) & V & W & U & W & V \\ V & v_\Gamma |\mathbf{k}_\parallel| \cos \varphi & V & W & U & W \\ W & V & v_\Gamma |\mathbf{k}_\parallel| \cos(\varphi + \frac{\pi}{3}) & V & W & U \\ U & W & V & -v_\Gamma |\mathbf{k}_\parallel| \cos(\varphi - \frac{\pi}{3}) & V & W \\ W & U & W & V & -v_\Gamma |\mathbf{k}_\parallel| \cos \varphi & V \\ V & W & U & W & V & -v_\Gamma |\mathbf{k}_\parallel| \cos(\varphi + \frac{\pi}{3}) \end{pmatrix} - i\gamma_0 \begin{pmatrix} 1 & \frac{1}{2} & -\frac{1}{2} & -1 & -\frac{1}{2} & \frac{1}{2} \\ \frac{1}{2} & 1 & \frac{1}{2} & -\frac{1}{2} & -1 & -\frac{1}{2} \\ -\frac{1}{2} & \frac{1}{2} & 1 & \frac{1}{2} & -\frac{1}{2} & -1 \\ -1 & -\frac{1}{2} & \frac{1}{2} & 1 & \frac{1}{2} & -\frac{1}{2} \\ -\frac{1}{2} & -1 & -\frac{1}{2} & \frac{1}{2} & 1 & \frac{1}{2} \\ \frac{1}{2} & -\frac{1}{2} & -1 & -\frac{1}{2} & \frac{1}{2} & 1 \end{pmatrix} \quad (\text{A2})$$

with  $\varphi = \arg(\mathbf{k}_\parallel)$ . Here the diffractive-coupling matrix is given by

At  $\mathbf{k}_\parallel = \mathbf{0}$ , diagonalizing  $\hat{H}(\mathbf{0})$  yields six eigenmodes.

Because the honeycomb geometry satisfies  $U < 0$ ,  $V < 0$ , and  $W < 0$ , the expression  $\Omega(0) = \omega_\Gamma + U + 2V + 2W$  is the lowest eigenvalue of the  $6 \times 6$  effective Hamiltonian

at the  $\Gamma$  point. This mode does not radiate at normal incidence, and therefore, it constitutes a symmetry-protected BIC that forms the parent Bloch resonance for all trapped states studied in this work. Its eigenvector is

$$\mathbf{A}(0) = (1, 1, 1, 1, 1, 1), \quad (\text{A3})$$

up to normalization: the six first-order harmonics oscillate in phase. The other five modes (two dipolar, two quadrupolar, one hexapolar) are described in detail in Ref. [17].

Expanding the eigenvalue to second order,

$$\Omega(\mathbf{k}_{\parallel}) \simeq \Omega(0) + \frac{v_{\Gamma}^2 k^2}{2(2U + V + 3W)} - i\gamma \frac{3v_{\Gamma}^2 k^2}{2(2U + V + 3W)^2}, \quad (\text{A4})$$

reveals an isotropic parabolic dispersion. Since  $2U + V + 3W < 0$ , the effective mass  $m = \hbar^2(2U + V + 3W)/v_{\Gamma}^2$  is negative, consistent with the experimental band curvature.

To linear order in  $k$ , the eigenvector becomes

$$\mathbf{A}(\mathbf{k}_{\parallel}) \simeq \mathbf{A}(0) + \frac{v_{\Gamma} k}{\sqrt{2}(2U + V + 3W)} \begin{pmatrix} \sin(\varphi + \frac{\pi}{6}) \\ \cos \varphi \\ -\sin(\varphi - \frac{\pi}{6}) \\ -\sin(\varphi + \frac{\pi}{6}) \\ -\cos \varphi \\ \sin(\varphi - \frac{\pi}{6}) \end{pmatrix}, \quad (\text{A5})$$

This generates a vortex-like angular dependence of the far field.

The electric field inside the slab (i.e. near field) follows

$$\mathbf{E}_{\text{near}}(\mathbf{r}_{\parallel}, z) = u(z) \sum_{n=1}^6 A_n(\mathbf{k}_{\parallel}) e^{i(\mathbf{G}_n + \mathbf{k}_{\parallel}) \cdot \mathbf{r}_{\parallel}} \mathbf{p}_n, \quad (\text{A6})$$

where  $u(z)$  is the vertically guided mode profile. For the monopolar BIC at  $\Gamma$ ,  $A_n(0) = 1$  for all  $n$ , giving

$$\mathbf{E}_{\text{near}}(\mathbf{r}_{\parallel}, z) \propto u(z) \sum_{n=1}^6 e^{i\mathbf{G}_n \cdot \mathbf{r}_{\parallel}} \mathbf{p}_n. \quad (\text{A7})$$

The magnetic field obtained from Maxwell's equations,

$$H_z(\mathbf{r}_{\parallel}, z) \propto u(z) \sum_{n=1}^6 e^{i\mathbf{G}_n \cdot \mathbf{r}_{\parallel}}, \quad (\text{A8})$$

produces a single-lobed, same-sign  $H_z$  distribution in each hexagonal unit cell, while the in-plane electric field  $\mathbf{E}_{\text{near}}(\mathbf{r}_{\parallel}, z)$  forms a circulating pattern around the cell center. This fully symmetric  $A_1$  texture — single-lobed  $H_z$  with circulating  $\mathbf{E}_{\parallel}$  is the origin of the term "magnetic monopolar".

In the single-channel regime, the radiated field is the guided-mode superposition projected onto the outgoing Fabry-Pérot channel,

$$\mathbf{E}_{\text{far}}(\mathbf{k}_{\parallel}) \propto \left[ \sum_n A_n(\mathbf{k}_{\parallel}) \mathbf{p}_n \right] \sqrt{\gamma(\mathbf{k}_{\parallel})}. \quad (\text{A9})$$

Using Eq. (A5) one obtains, to lowest order in  $k$ ,

$$\mathbf{E}_{\text{far}}(\mathbf{k}_{\parallel}) \propto k \begin{pmatrix} -\sin \varphi \\ \cos \varphi \end{pmatrix} = k \hat{\mathbf{u}}_{\varphi}, \quad (\text{A10})$$

and therefore

$$\mathbf{E}_{\text{far}}(\mathbf{0}) = \mathbf{0}. \quad (\text{A11})$$

This confirms that the monopolar mode is a symmetry-protected BIC of topological charge +1 at  $\Gamma$ .

### Experimental setup for farfield measurements

Energy-momentum dispersions were measured using a custom-built back-focal-plane (BFP) imaging setup. The Fourier plane of a  $\times 100$  microscope objective (NA = 0.8) was imaged onto the entrance slit of a grating spectrometer (HRS-500MS-NI, Princeton Instruments). The sample was mounted such that its  $x$ -axis, corresponding to the  $\Gamma$ - $K$  direction of the honeycomb lattice, was aligned with the slit. The spectrum dispersed by the grating was detected using a two-dimensional InGaAs camera (NIRvana HS, Princeton Instruments), providing simultaneous access to  $k_x$  and optical energy. To measure the  $\Gamma$ - $M$  dispersion, the sample was rotated such that its  $y$ -axis aligned with the slit, providing access to  $k_y$ . Angle-resolved reflectivity [Fig. 2(d)] and angle-resolved photoluminescence [Figs. 3(b) and 5(b)] are acquired using the same setup but with different illumination sources: a broadband halogen lamp for reflectivity and a femtosecond laser (800nm, Coherent Chameleon Ultra II) for photoluminescence.

Real-space and momentum-space far-field intensity and polarization maps [Figs. 2(e-g), 4(d-g), and A1] are obtained on the same optical platform operated in a tomographic configuration, in which either the BFP plane or the object plane was scanned relative to the spectrometer slit while selecting different polarization analyzers. This method, which yields quantitative polarization-resolved images in both  $(k_x, k_y)$  and  $(x, y)$ , is described in detail in our previous study [31].

### Determination of the potential amplitude $V_0$

In Eqs. (1) and (3), the far-field polarization of the underlying monopolar Bloch resonance is fixed,  $\mathbf{E}_{\text{far}}(\mathbf{k}_{\parallel}) \propto k \hat{\mathbf{u}}_{\varphi}$ . As a result, the pump-induced reconfiguration of both the near- and far-field distributions is governed solely by the envelope function of the trapped state. We obtain this envelope numerically by solving the two-dimensional Schrödinger equation

$$-\frac{\hbar^2}{2m} \nabla_{\mathbf{r}_{\parallel}}^2 F(\mathbf{r}_{\parallel}) + V(\mathbf{r}_{\parallel}) F(\mathbf{r}_{\parallel}) = E F(\mathbf{r}_{\parallel}), \quad (\text{A12})$$

where  $F(\mathbf{r}_{\parallel})$  is the envelope (wavefunction),  $V(\mathbf{r}_{\parallel})$  is the effective potential, and  $E$  is the eigenenergy.

For single-spot pumping we model the carrier-induced potential as a Gaussian,

$$V(\mathbf{r}_{\parallel}) = V_0 \exp\left(-\frac{|\mathbf{r}_{\parallel}|^2}{\sigma^2}\right), \quad (\text{A13})$$

characterized by the pump waist  $\sigma$  and the potential amplitude  $V_0$ . The waist  $\sigma$  is extracted experimentally from a Gaussian fit to the real-space pump-intensity profile on the sample. The amplitude  $V_0$  is then treated as a fitting parameter and tuned until the eigenenergy obtained from the Schrödinger solver matches the confinement energy  $\Delta E$  measured in the saturated regime [Fig. 3(d)].

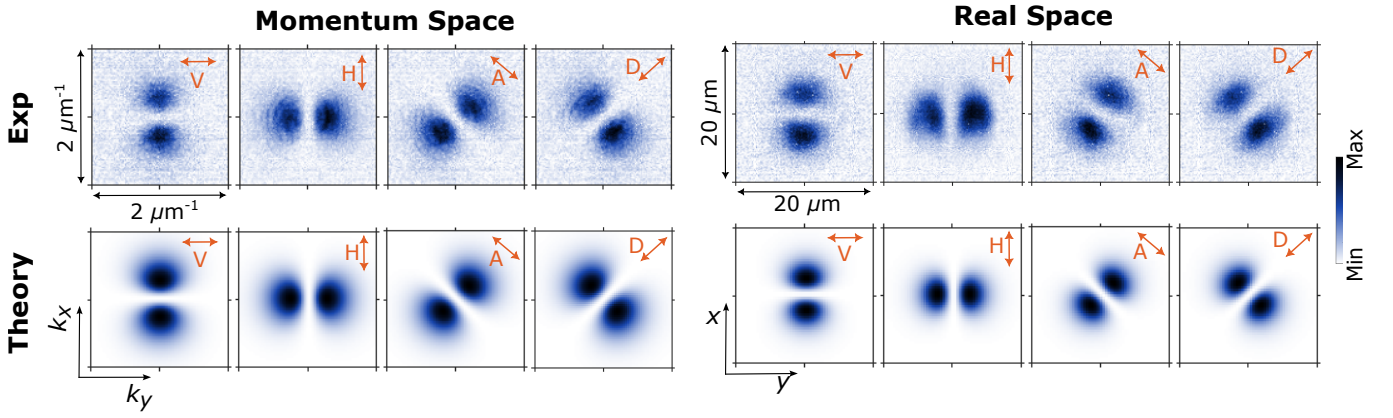


Figure A1. **Polarization maps for single pump** Experimental and Theoretical polarization resolved farfield lasing images in real and momentum space, for pump waist  $\sigma = 3.2 \mu\text{m}$  with a linear polarizer in front of the InGaAs camera (Methods). The polarizer is rotated  $0^\circ$  (H),  $45^\circ$ (D),  $90^\circ$ (V),  $125^\circ$ (A). [Refer fig.3(e-h)] for images without a polarizer.]

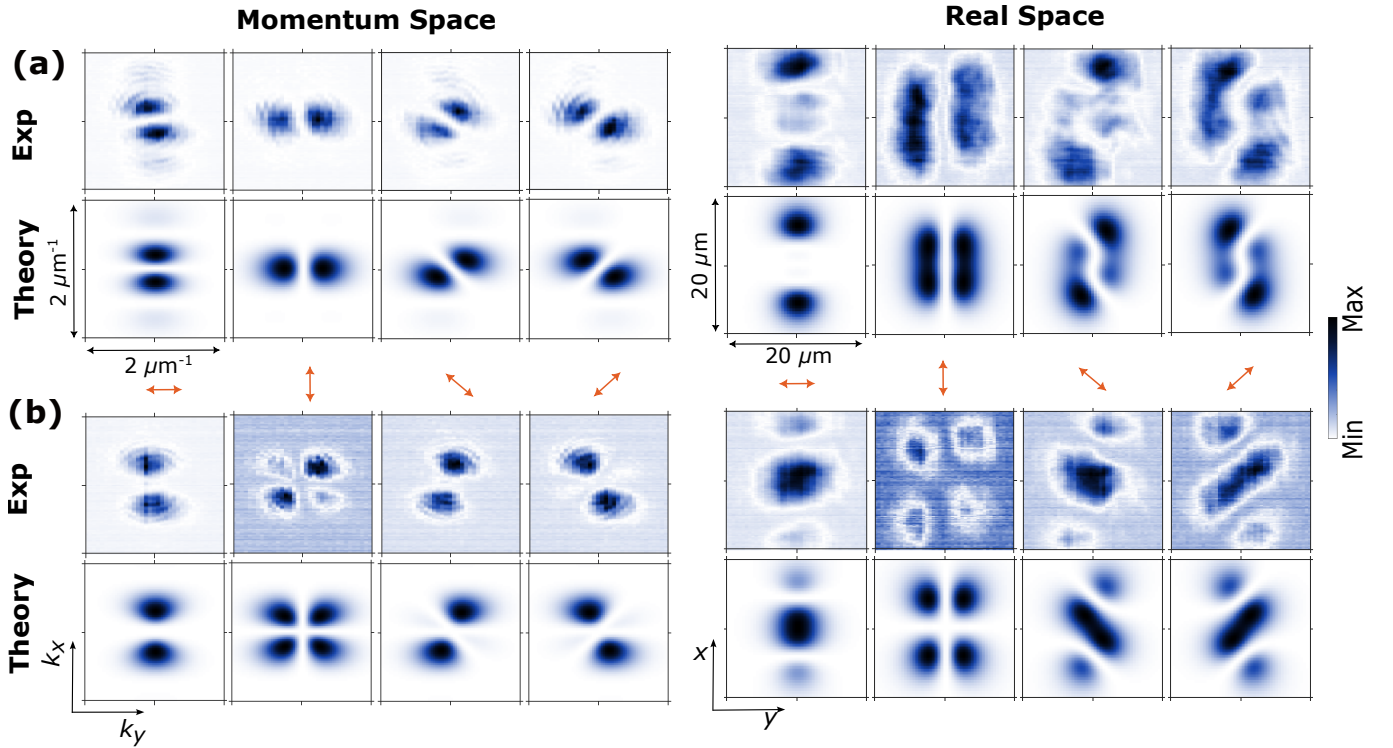


Figure A2. **Polarization maps for double pump spot:** Polarization-resolved far-field lasing images for (a) bonding and (b) antibonding modes in real and momentum spaces, for images shown in fig.5(d-g). The polarizer is rotated  $0^\circ$ ,  $45^\circ$ ,  $90^\circ$ ,  $125^\circ$ . The top and bottom panel show the experimental and analytical results respectively.

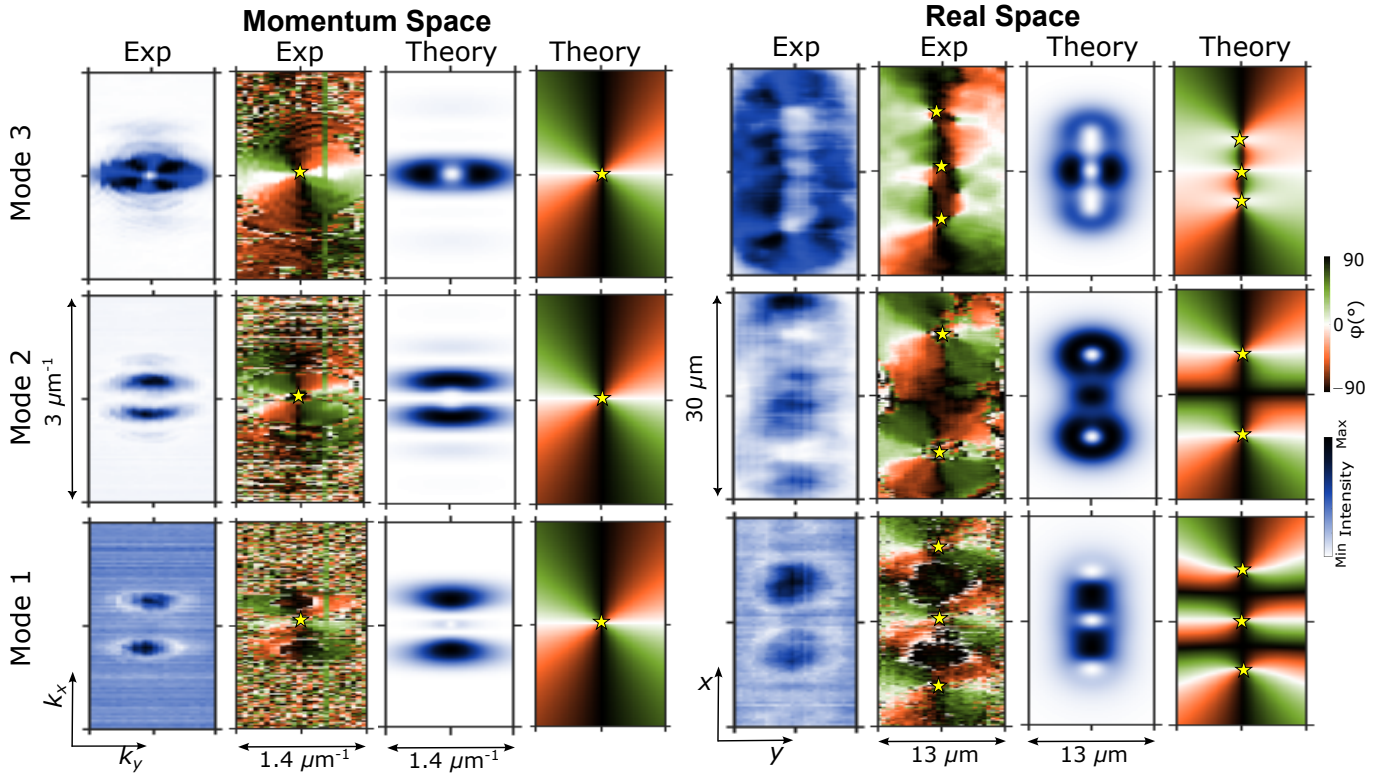


Figure A3. **Three-spot pumping and multi-singularity trapped modes.** Experimental and theoretical far-field characterization of the three trapped modes formed under three-spot pumping with spot separation  $L = 13 \mu\text{m}$  and spot size  $\sigma = 2.5 \mu\text{m}$ . Each row corresponds to one of the three trapped eigenstates supported by the triple-well potential. For each mode, the panels show (from left to right): experimental real-space intensity, experimental real-space polarization texture, theoretical real-space intensity, theoretical real-space polarization texture. The same sequence is used for the momentum-space emission. The number and spatial arrangement of real-space polarization singularities (yellow stars) directly follow from the nodal structure of the pump-induced envelope function: one singularity for the ground state (Mode 1), two for the first excited state (Mode 2), and three for the second excited state (Mode 3). In contrast, all modes preserve the same momentum-space vortex at  $\Gamma$ , inherited from the monopolar BIC of the underlying Bloch resonance.